Optics and Lasers in Engineering 175 (2024) 108002

Contents lists available at ScienceDirect

Optics and Lasers in Engineering

journal homepage: www.elsevier.com/locate/optlaseng

Revisiting the sample transmittance and camera bit-depth effects on quantitative phase imaging in off-axis digital holographic microscopy

C. Buitrago-Duque [a], J. Garcia-Sucerquia [a], M. Martínez-Corral [b], E. Sánchez-Ortiga [c,*]

[a] Universidad Nacional de Colombia Sede Medellín, School of Physics, A.A: 3840, Medellín 050034, Colombia
[b] 3DDI Laboratory, Department of Optics, University of Valencia, Burjassot E46100, Spain
[c] Centro de Tecnologías Físicas, Universitat Politècnica de València, Valencia E-46022, Spain

ARTICLE INFO

Keywords:
Digital holography
Microscopy
Phase imaging

The performance of single-shot off-axis digital holographic microscopy (DHM) is determined by the optimum utilization of the space-bandwidth product and by the contrast of the recorded digital hologram. While the former can be easily achieved through an afocal-telecentric DHM, the finding in nature of samples with non-homogeneous transmittance leads to the recording of digital holograms with contrast ranging from zero to unity. In this work, the effect of the sample transmittance and the bit depth of the digital camera on the performance of quantitative phase imaging in DHM is studied. A theoretical model that links the contrast of the recorded interference fringes, in a transmission-mode DHM, to the bit depth of the digital camera is derived. The model is implemented in an open-source visual script for easy consultation and predicts that, when recorded with a 16-bit-depth camera, digital holograms of samples that have regions with transmittance below 1% can be successfully processed to render reliable phase information. The theoretical and computer-modeled results are validated with experimental results from a complex sample of the mouth of a honeybee and from endothelial cells slide.

1. Introduction

Quantitative phase imaging (QPI) of microscopic samples plays a key role in material and life sciences [1]. In the former, reflective samples are imaged in microscopes operating in reflection mode to accurately measure high differences. In life sciences, transmissive specimens are imaged in microscopes operating in transmission mode to quantify the phase differences between the specimen and the surrounding medium. Among the multiple methodologies to implement QPI, digital holographic microscopy [2–4] (DHM) has attracted special interest because of its intrinsic simplicity of implementation, ample amount of information available, commercial and open-source developments of hardware [5–7] and software [8–10], and the reliable results that can be obtained.

The hallmark of DHM is the single-shot label-free QPI capability for both reflective and transmissive samples. While heights with nanometric sensitivities have been successfully measured in the reflection mode [11,12], in DHM operating in transmission mode phase differences have been measured with sensitivities of fractions of hundredths of radians [3,11,13,14]. DHM is based on recording on a digital camera the amplitude superposition between an object wave and a reference wave. The former corresponds to the complex-valued wavefield scattered by the object that is imaged at the camera plane, and the latter is usually chosen to be a plane wave impinging with a given angle to the plane of the digital sensor. The squared modulus of this amplitude superposition, known as the digital hologram, can then be digitally processed to retrieve the complex-valued amplitude scattered by the sample at the sensor plane. This complex-valued wavefield can also be calculated at different depth planes by means of a numerical propagation based on the scalar diffraction integral [15–17]. This feature gives DHM an a-posteriori numerical depth of focus [18–20] well-suited, for instance, for particle velocity studies [21].

Different methods can be utilized to retrieve the complex-valued object wavefield from the digital hologram. For DHM to operate in a single-shot approach, the microscope must be arranged in an off-axis architecture [2,4,22,23]. When operating off-axis, the best possible DHM configuration is an afocal-telecentric arrangement, which guarantees that the retrieved object complex-valued wavefield is not affected by the phase curvature introduced by the imaging microscope objective and that the optimal optical performance of the microscope is reached [23–25]. For this configuration, the numerical aperture and magnification of the microscope objective, the pixel size of the digital

* Corresponding author.
E-mail address: emilio.sanchez@uv.es (E. Sánchez-Ortiga).

https://doi.org/10.1016/j.optlaseng.2023.108002
Received 16 March 2023; Received in revised form 21 September 2023; Accepted 21 December 2023
Available online 5 January 2024

camera, and the interference angle between the object and the reference waves must be finely chosen, as is clearly described elsewhere [23]. Operating in an afocal-telecentric configuration the retrieving of the object complex-valued wavefield is easily done by spatial filtering in the Fourier domain [26–28], a task for which even automatic methods are widely available [28,29]. The performance of the spatial filtering method depends, to a large extent, on having a Fourier spectrum with non-overlapping diffracted orders that can be easily isolated. The precise setup in the afocal-telecentric arrangement [23] guarantees an optimized use of the space-bandwidth product in terms of the location of the diffracted orders. On the contrary, the contrast of the interference fringes of the digital hologram controls their weight, namely, how visible they are in the Fourier spectrum. Conventionally, as inherited from optical holography [30], the said contrast is sought to be unitary, which is achieved by tunning the intensity ratio between the object and reference waves; the closer the contrast is to unity, the easier and more precise the recovery of the complex-value wavefield can be done. For a reflection-mode DHM, the digital hologram can be set up at contrast values close to unity with relatively low effort. However, in transmission-mode DHM, the local variations of the sample transmittance make it challenging or outright impossible to have a homogeneous and global contrast value of the digital hologram all over the sample. Indeed, it is possible to even have nearly opaque object regions with near-zero contrast in the corresponding interference fringes.

In this work, the effect of the sample transmittance and the bit depth of the digital camera on the performance of QPI in digital holographic microscopy is reported. Even though previous works have studied the performance of DHM operating at very weak signals and under alternative architectures [14,22,31–36], most of them are focused on intensity images. To the best knowledge of the authors, there is no reported study on the combined influence of both effects. Herein, a theoretical model that quantifies the interference fringes contrast, in a transmission mode single-shot DHM, and that links it to the bit depth of the digital camera is derived. The main outcomes from the model are two predictions: First, that even in object regions with transmittances below 1 % it is possible to recover reliable phase information. And second, that holograms from translucent samples can be well represented in a reduced bit depth without detriment to the quantitative phase map. The simulated and experimental results confirm the validity of the model and these two predictions.

2. Fundamentals of Digital Holographic Microscopy: Digital Hologram Contrast and Quantization

The common arrangement of an off-axis DHM operating in an afocal-telecentric configuration [23] is illustrated in Fig. 1. The distance between the microscope objective (*MO*), and the tube lens (*TL*), equals the sum of their focal distances $f_{MO}.f_{TL}$, in that order. The digital camera records the squared modulus of the amplitude superposition of the object wave, $O_i(\vec{x})$, and the reference wave, $R(\vec{x})$,

$$I(\vec{x}) = |\alpha_o O_i(\vec{x}) + \alpha_r R(\vec{x})|^2; \tag{1}$$

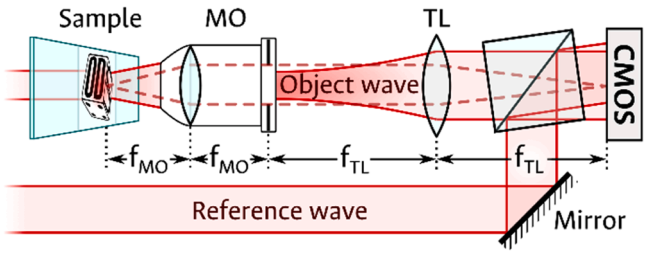

Fig. 1. Schematic illustration of an off-axis DHM. MO = Microscope objective, TL = Tube lens.

with $\vec{x} = (x, y)$ being the transverse coordinates of the system at the imaging plane and where $\alpha_o$and α_r are constants that allow precise scaling of the amplitudes of the object and reference waves, respectively. The object wave is the coherent image of the sample at the digital sensor plane [15], as given by

$$O_i(\vec{x}) = O\left(\frac{\vec{x}}{M}\right) \otimes h(\vec{x}) = t(\vec{x}) e^{i\phi(\vec{x})}. \tag{2}$$

In Eq. (2), $\otimes$ is the 2D convolution, $h(\vec{x})$ is the amplitude impulse response of the microscope, and $M = -f_{TL}/f_{MO}$ is the lateral magnification of the microscope. $O(\frac{\vec{x}}{M}) = t_o(\frac{\vec{x}}{M}) e^{i\phi_o(\frac{\vec{x}}{M})}$ is a complex-valued quantity that accounts for the spatially distributed transmittance, $t_o(\frac{\vec{x}}{M})$, and phase, $\phi_o(\frac{\vec{x}}{M})$, of the sample at the object plane. The reference wave is generally considered a plane wave that impinges on the digital sensor traveling at the angle given by the tilted beam-splitter; this angle can be represented by the wave vector $\vec{k}$, such that

$$R(\vec{x}) = A(\vec{x}) e^{i\vec{k}\cdot\vec{x}}, \tag{3}$$

where $A(x)$ describes the amplitude spatial distribution of the reference wave. Explicitly writing Eq. (1) yields [37],

$$\begin{aligned} I(\vec{x}) &= \alpha_o^2 t(\vec{x})^2 + \alpha_r^2 A(\vec{x})^2 + 2\alpha_o \alpha_r t(\vec{x}) A(\vec{x}) \gamma \cos\left(\vec{k}\cdot\vec{x} - \phi(\vec{x})\right) \\ &= (\alpha_r A(\vec{x}))^2 \left[1 + \left(\frac{\alpha_o t(\vec{x})}{\alpha_r A(\vec{x})}\right)^2 + 2\gamma \frac{\alpha_o t(\vec{x})}{\alpha_r A(\vec{x})} \cos\left(\vec{k}\cdot\vec{x} - \phi(\vec{x})\right)\right] \end{aligned} \tag{4}$$

with γ being the complex degree of spatial coherence that accounts for the capability of the object and reference waves to interfere [38], thus determining to a great extent the contrast of the fringes of the digital hologram. For conciseness, and without any lack of generality, the analysis to follow is restricted to the one-dimensional case, whose extension to two dimensions is straightforward. As the digital hologram in Eq. (4) is recorded in a digital camera with a pixel of size Δx the m^{th} pixel records an intensity given by

$$I_m = \int_{\left(m-\frac{1}{2}\right)\Delta x}^{\left(m+\frac{1}{2}\right)\Delta x} \frac{I(x)}{\Delta x} dx. \tag{5}$$

For the calculation in Eq. (5), one can consider that both the object and reference waves are smooth enough over the pixel area, such that $A(x)$, $t(x)$, and $\phi(x)$ are approximately constant across the length $\left[x - \frac{\Delta x}{2}, x + \frac{\Delta x}{2}\right]$. Upon this consideration,

$$I_m = (\alpha_r A(x))^2 \left[1 + \left(\frac{\alpha_o t(x)}{\alpha_r A(x)}\right)^2 + 2\gamma \frac{\alpha_o t(x)}{\alpha_r A(x)} \operatorname{sinc}\left(\frac{k\Delta x}{2}\right) \cos(km\Delta x - \phi(x))\right]. \tag{6}$$

with $\operatorname{sinc}(\ldots) = \frac{\sin(\ldots)}{(\ldots)}$. By defining $r(x) = \frac{\alpha_o t(x)}{\alpha_r A(x)}$ as the ratio of the relative amplitudes of the reference and the object waves, eq. (6) can be written as.

$$I_m = (\alpha_r A(x))^2 \left[1 + (r(x))^2 + 2\gamma r(x) \operatorname{sinc}\left(\frac{k\Delta x}{2}\right) \cos(km\Delta x - \phi(x))\right]. \tag{7}$$

In Eq. (7), the intensity recorded in the m^{th} pixel is expressed in terms of the parameters that control the contrast of the digital hologram; namely, γ, r, and the modulation transfer function (MTF) of the digital camera with a pixel fill factor of 1, $\operatorname{sinc}\left(\frac{k\Delta x}{2}\right)$ [39]. From Eq. (7), the contrast of the digital hologram, defined as Michelson's visibility [40], for the case of $t(x)$ and $A(x)$ as constants, is given by

$$V(x)=\frac{[I_m]_{max}-[I_m]_{min}}{[I_m]_{max}+[I_m]_{min}}=2\gamma\frac{r(x)}{1+r(x)^2}\ \mathrm{sinc}\left(\frac{k\Delta x}{2}\right). \tag{8}$$

The visibility of the digital holograms is therefore controlled by the complex degree of spatial coherence and the amplitude ratio between the interfering object and reference waves. The MTF of the digital sensor modulates the said visibility, indicating that the larger the pixel size the smaller their effect on the visibility. This condition indicates that, to keep the best possible balance between the angle of interference of the object and the reference waves and the MTF of the digital camera, a detailed design of the DHM microscope must be considered. The angle must be small enough to guarantee the correct sampling of the digital hologram and large enough to produce the smallest possible penalization on the contrast of the digital hologram by the MTF.

In order to consider the recording of a digital hologram with the visibility expressed in Eq. (8), the quantized nature of the recorded intensity by the digital sensor must be taken into account. I_m is limited to have values $q(m\Delta x)$ within the interval $\{q(m\Delta x)\in\mathbb{R},\ 0\le q(m\Delta x)\le 2^b-1\}$, with b being the bit depth of the digital sensor's analog-to-digital converter, and $\mathbb{R}$ the set of real numbers. This value range is determined by engineering parameters of the sensor like its exposure time, electronic gain, and gamma factor, among others. Several conditions can thus be imposed to simplify modeling the quantization process: i) the sensor has a linear response with the intensity, ii) the lowest gray level of the registered hologram is zero, corresponding to the sensitivity threshold of the sensor, iii) the sensor parameters can be adjusted so that the maximum intensity in the sensor plane corresponds to the largest gray level of the registered image, and iv) the sensor cannot reach its saturation limit. Under these considerations, the $q(m\Delta x)$ value for the position $m\Delta x$ is therefore given by

$$q(m\Delta x)=I_m(m\Delta x)\frac{2^b-1}{[I_m]_{max}}, \tag{9}$$

where $[I_m]_{max}=(\alpha_r A(x))^2[1+r(x)^2+2\gamma r\mathrm{sinc}(k\Delta x/2)]$, is the maximum intensity of the digital hologram. The value of $q(m\Delta x)$ must now be quantized to one of the integer numbers $\mathbb{Z}$ within the range $\{q_m\in\mathbb{Z}\wedge 0\le q_m\le 2^b-1\}$. To do so, the ceiling operator $\lceil f\rceil$ maps f to the nearest integer greater than or equal to f; explicitly, $\lceil f\rceil.=i:i\in\mathbb{Z}\wedge i\ge f\wedge\{\forall j>f:j\in\mathbb{Z},\ i\le j\}$. The application of the ceiling operator to eq. (9) yields

$$q_m=\left\lceil(2^b-1)\frac{1+r(x)^2+2\gamma\ r(x)\mathrm{sinc}\left(\frac{k\Delta x}{2}\right)\cos(km\Delta x-\phi(x))}{1+r(x)^2+2\gamma\ r(x)\ \mathrm{sinc}\left(\frac{k\Delta x}{2}\right)}\right\rceil \tag{10}$$

for the quantized value of the recorded intensity of the digital hologram.

At the core of the herein presented study is the non-homogeneous transmittance of the specimens imaged in DHM. The dimensionless parameter $r(x)$ introduced in the derivation of Eq. (10) allows the analysis of highly inhomogeneous samples that might include both transparent, $t(x)=1$, and totally opaque, $t(x)=0$, regions. The spatially distributed values for the r parameter describe the also spatially distributed intensity of the digital hologram. The maximum quantized intensity possible is still bounded by $q_m=2^b-1$, which represents the saturation level of the detector for the case of total transparency of the sample $t(x)=1$. Consequently, the maximum real value of the intensity recorded by the detector, when the amplitude of the reference wave is unitary $A(x)=1$, reduces to

$$[I_m]_{max}=(\alpha_r)^2\left[1+r_\alpha^2+2\gamma r_\alpha\mathrm{sinc}(k\Delta x/2)\right] \tag{11}$$

with $r_\alpha=\alpha_o/\alpha_r$ constant. This, in turn, allows the quantized value q_m in Eq. (10) to be rewritten as

$$q_m=\left\lceil(2^b-1)\frac{1+r(x)^2+2\ \gamma\ r(x)\ \mathrm{sinc}\left(\frac{k\Delta x}{2}\right)\cos(km\Delta x-\phi(x))}{1+r_\alpha^2+2\gamma r_\alpha\mathrm{sinc}\left(\frac{k\Delta x}{2}\right)}\right\rceil \tag{12}$$

whose values are equally limited as those in Eq.(10).

These quantized intensity values form the digital hologram from which the QPI information is retrieved. The reconstruction is carried out by spatial filtering of the digital hologram to isolate one of the diffracted orders [26], from which the complex-valued wavefield at the detector plane is retrieved. Under the afocal-telecentric configuration, the sample is imaged in focus and, consequently, the retrieved complex-valued amplitude can be directly used to compute any of the sample's wavefield properties, like its intensity or phase distribution [4,23]. In particular, the phase information is codified in the distortion of the carrier fringes. Thus, this reconstruction method is supported by the possibility of detecting these distortions in the resulting pattern from the interference between the reference and the object waves. It is therefore necessary to evaluate how many q_m values are needed to adequately represent the range of quantized intensity of the digital hologram. The limit values of the fringe pattern can be determined from a pair of π-shifted phase values of the sample. If the whole range of the fringe intensity values must be represented in at least NL quantized values in the digital hologram, it follows that

$$q_m|_{\varphi=0}-q_m|_{\varphi=\pi}\ge NL, \tag{13}$$

where $\varphi=km\Delta x-\phi(m\Delta x)$. Replacing the corresponding values of $q_m|_{\varphi=0}$ and $q_m|_{\varphi=\pi}$,

$$\left\lceil\mathscr{C}+(2^b-1)\frac{2\ \gamma\ r\ \mathrm{sinc}\left(\frac{k\Delta x}{2}\right)}{1+r_\alpha^2+2\gamma r_\alpha\mathrm{sinc}\left(\frac{k\Delta x}{2}\right)}\right\rceil-\left\lceil\mathscr{C}-(2^b-1)\frac{2\ \gamma\ r\ \mathrm{sinc}\left(\frac{k\Delta x}{2}\right)}{1+r_\alpha^2+2\gamma r_\alpha\mathrm{sinc}\left(\frac{k\Delta x}{2}\right)}\right\rceil\ge NL \tag{14}$$

where

$$\mathscr{C}=(2^b-1)\frac{1+r^2}{1+r_\alpha^2+2\gamma r_\alpha\mathrm{sinc}(k\Delta x/2)}\ . \tag{15}$$

A limit case that is customarily performed at the laboratory is the use of fully spatially coherent light sources, like laser light, for which $\gamma=1$. Additionally, the tunning of the relationship between the reference and the object wave illumination can be chosen to be unitary, $r_\alpha=1$, and the digital hologram can be assured to be sampled at the Nyquist limit [15] such that $\Delta x=\pi/k$. For these conditions, Eq. (14) reduces to

$$\lceil 0.3055(2^b-1)(1+\beta^2+1.2732\beta)\rceil-\lceil 0.3055(2^b-1)(1+\beta^2-1.2732\beta)\rceil\ge NL \tag{16}$$

with $\beta(x)=\frac{t(m\Delta x)}{A(m\Delta x)}$ being bounded between zero and one $0\le\beta\le 1$. Both equations, (14) and (16), for general and a particular case, indicate the tight link between the number of quantized levels in which the digital hologram is recorded, NL, and the physical parameters that influence the performance of any QPI measurement in DHM. To provide further insight into this regard, as part of the present work, a MATLAB® Live Script resource that plots eq. (14) while allowing the user to modify the experimental parameters at will, was made available at Ref. [41].

Presented in Fig. 2 are different plots for a particular set of parameters of interest for the current work. The complex degree of coherence

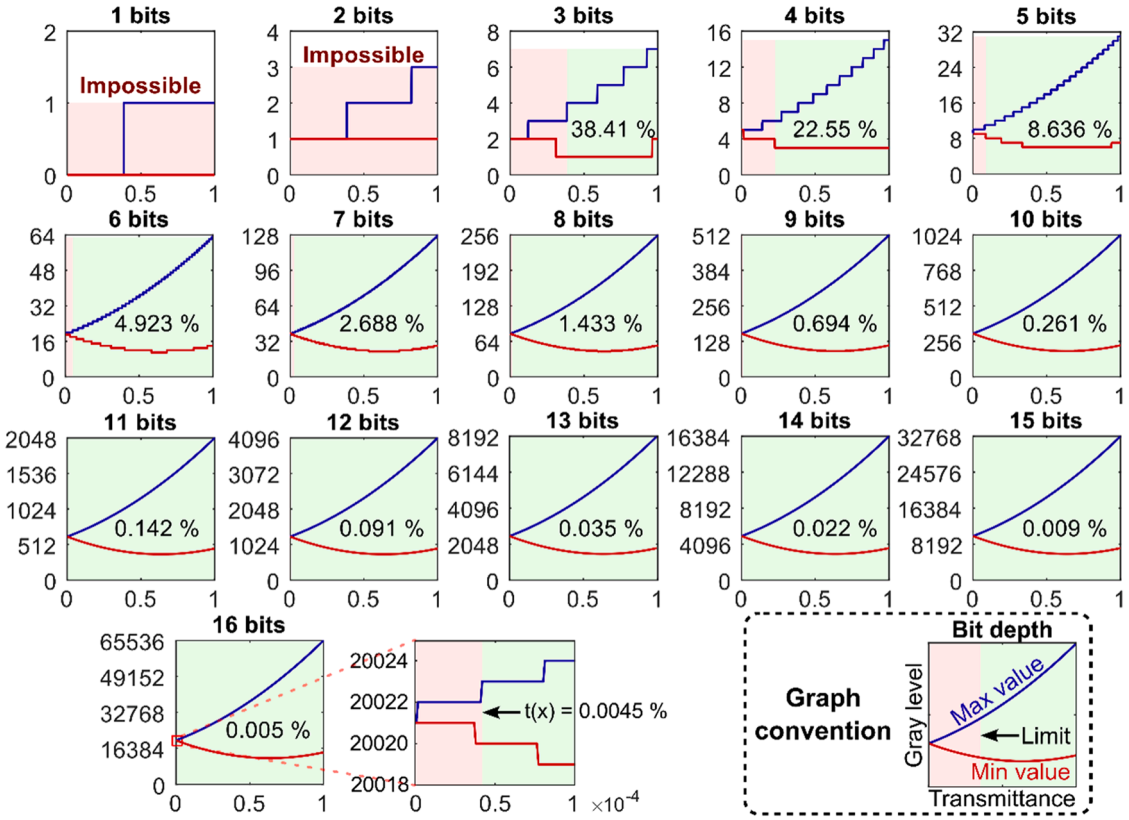

Fig. 2. Sample transmittance vs Quantization levels. All the panels use the graph convention illustrated in the lower-right corner. See the text for details.

has been set to one, $\gamma = 1$, for representing the full spatial coherence of the utilized laser light. Each panel plots the sample transmittance $t(x)$ vs the number of levels in which the digital hologram is quantized. The amplitude of the reference wave $A(x)$ is chosen to be uniform, and at a 1:1 intensity relation with the object illumination as given by $r_\alpha = 1$. The number of the available quantization levels is therefore determined by the bit-depth of the digital camera, which is shown at the top of each panel. The MATLAB® Live Script resource allows choosing the number of levels *NL* that satisfies the condition stated in Eq. (14). For the modeling shown in this figure *NL* has been set to 3. This value has been experimentally found as the best fit for the experimental observations when coherent noise also affects the measurements. It shows good compliance with the realistic numerical modeling presented in the next section. The blue and red stepped lines denote the maximum and minimum values, in that order, of the quantized digital hologram. Note that, from now on, the transmittance of the object is represented as the proportion of transmitted light. The MATLAB® Live Script resource evaluates the fulfillment of the *NL* condition and represents it by shading in red the region of the plotting area where it fails; the remaining area is green-shaded to indicate the fulfillment of the condition. The boundary between these areas marks the limit sample transmittance for which the digital hologram can correctly record, and allow the retrieval, of a trustable QPI map. Remarkable conclusions can be extracted from the panels in Fig. 2. For example, when a regular 8-bit camera is utilized to record the digital hologram, thrustable QPI images from samples with transmittances as low as 1.4% can be obtained. In the case of using a 16-bit camera, the sample transmittance can be as low as 0.005 %. Conversely, the model predicts that holograms from fully transmissive samples could be appropriately represented in as low as 3 bits without affecting the possibility of retrieving their phase information.

Most commercially available digital cameras integrate at least 8-bit analog-to-digital converters, with 12-bit and 16-bit sensors being increasingly common. The results from this model thus suggest that a DHM system equipped with a modern camera could retrieve information from almost opaque samples, possibly around 1 % of transmittance. It must be noted that these enhancements in the intensity quantization resolution come at the expense of an increased size of the digital files, which demand the use of high-capacity and bandwidth storage for time-extended DHM imaging. However, from these same observations, the model suggests that if translucent samples are being studied, as is commonly the case for DHM applications, the recordings could be saved in a compressed representation without affecting the QPI capabilities of the technique. Consequently, new compression algorithms could be developed under this principle [42,43]. These figures thus encourage the numerical modeling of QPI imaging in realistic platforms [10,29,44] and the realization of experiments with transmissive samples exhibiting remarkably low values, and the compressed representation of fully transmissive targets.

The specific values that motivate these observations are based on the calculation with $NL = 3$. In its current form, this value is experimentally estimated rather than deduced. However, the predictions of the model are equally valid for other near values of *NL*. This can be readily tested in the supplementary software tool [41]. In particular, the predicted transmittance limits for the most common camera sensors (that is, equal to or above 8 bits) are only slightly changed by either increasing or decreasing the *NL* value in one unit. Likewise, the observation that holograms from fully transmissive samples can be accurately represented in as low as 3 bits holds without issue for that same uncertainty.

3. Numerical Modeling

To validate the proposed theoretical model, the transmittance limits predicted by Eq. (14) and summarized in Fig. 2 were evaluated through a numerical recreation of a DHM recording setup. The realistic simulation platform reported in [10,44] was employed to produce digital holograms with bit-depth representations varying from 1-bit to 16-bit.

The recording system was assumed to operate with a fully-coherent 633 nm illumination, to use 10x/0.25 microscope objective, and to record in a digital sensor with 1080 × 1080 square pixels with 5.04 μm of side length. As the sample target for this simulation, the synthetic phase object illustrated in panel (a) of Fig. 3 was used. This object was designed as 9 identical phase structures with a difference of 2 radians between the flat top and the background, thus being of equal optical path length. A different value of transmittance was assigned to each of the structures, ranging from 80 % to 0 % in 10 % decrements, and keeping a 100 % translucent background. The resulting 16-bit hologram is shown in panel (b) of the same figure. From the accompanying insets is seen that the fringe contrast inside the regions corresponding to the imaged structures decreases with the reduced transmittance. As the quality of the phase maps retrieved from these holograms depends on the possibility of adequately representing the fringe pattern over the available intensity levels, perturbations are bound to appear as the bit depth is decreased. Indeed, this effect can be seen comparing panels (c), (d), and (e). Panel (c) shows the phase map retrieved from the 16-bit representation; as expected, all the non-zero-transmittance structures are correctly retrieved without any perturbation. Panel (d) shows the reconstruction from the 4-bit hologram, in which the structures above 50 % are retrieved without distortion, those between 40 % and 10 % have partially altered shapes, and only the 0 % structure is severely corrupted. Conversely, panel (e) shows the reconstruction from the 2-bit hologram, in which none of the structures is adequately recovered, those between 80 % and 30 % are altered in various degrees, and those below 20 % are indistinguishable. In these last three panels, the green, yellow, and red arrows mark the transitions between elements that are, respectively, correctly retrieved without perturbation, retrieved with partial alterations, and those for which the phase information is unretrievable.

This described experiment was then repeated for transmittances between 8 % and 0 % with 1 % variations, 0.8 % to 0 % with 0.1 % variations, and 0.08 % to 0 % with 0.01 % variations. For each simulation, the same 16 cases of bit-depth representations were generated and reconstructed. To quantify the affectations on the retrieved phase, the standard deviation of the phase values was measured in the flat top region of the structures, which was represented in each case by approximately 80 × 80 pixels of the phase map. These measurements were then used to plot the trends illustrated in Fig. 4. To establish the maximum acceptable value, the standard deviation of the background was taken as the reference. For the selected simulation conditions, the average deviation of this 100 % transmissive region was measured at 0.01 rad. The transmittance limit was estimated by the position where the trends exceeded the acceptable deviation range, that is, if the measured standard deviation surpassed more than two times that of the background. While the results, which are summarized as annotations in the corresponding panel of Fig. 4, predict slightly higher limits for the limit transmittance values, the overall behavior is consistent with the theoretical model. Namely, that 16-bit recordings allow the phase retrieval from regions of the sample with transmittances below 0.1 %, and that translucent regions can be adequately represented with bit-depths as low as 3-bit. These observations must now be further validated in an experimental setting.

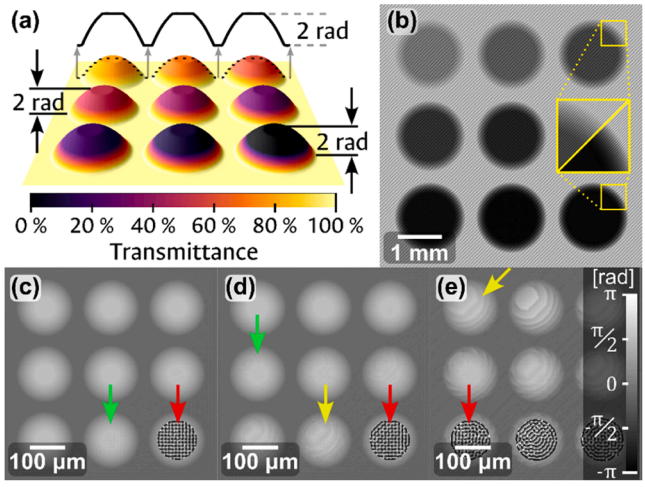

Fig. 3. Modeled object for numerical estimation of transmittance limits. (a) 3D representation of the simulated sample, composed of 9 equal-phase elements with transmittances varying from 80% to 0%. (b) Resulting 16-bit hologram. The insets show the difference in fringe contrast between the two regions with 60% and 0% transmittance. Presented in c/d/e panels are the reconstructed phase maps with non-/partially-/fully-distorted features for holograms with 16-bit/4-bit/2-bit. In these panels, the green, yellow, and red arrows indicate the transition between fully-recovered, partially-recovered, and unrecoverable phase values, respectively. The phase color scale bar applies to the three panels.

4. Experimental Validation

From the described model, two observations can be readily drawn regarding single-shot DHM quantitative phase imaging: i) imaging of highly opaque regions of a transmission sample can be sought if a camera with a high enough bit-depth range is employed, and ii) phase maps of a translucent sample can be retrieved from low-bit-depth holograms.

To verify these observations, a calibration phase-only target [45] was initially used. This sample is fabricated from an acrylate polymer deposition over a Corning Eagle XG glass substrate, making it a pure-phase object and, thus, fully transmissive. As the polymer depositions are height-calibrated and the refractive index of the material is accurately known, the phase delays introduced by the target can be readily predicted and used as a quantitative reference for phase retrieval under extreme conditions of sample transmittance. The sample is composed of several calibration structures. For this experiment, a 40-spoke Siemens star with 200 nm of height and 400 µm of diameter was selected. All the experimental recordings were performed in a single-shot DHM operating in an afocal-telecentric setup. The DHM was configured with a 633 nm laser illumination source, a 10X/0.25 microscope objective, and a passively-cooled Quantalux monochrome sCMOS camera (CS2100M-USB). The object and reference paths of the DHM were set in a 1:1 relation of intensities at the detector in the absence of a sample; that is, $\alpha_o/\alpha_r \approx 1$. The digital sensor was composed of 1920 × 1080 square pixels with 5.04 μm of side length, each with a full-well capacity of at least 23 000 e^-, and it was equipped with a 16-bit ADC with less than 1.5 e^- RMS.

For the first observation, due to the translucent nature of this sample, an emulation of low transmittance values had to be sought. To do so, the object arm of the DHM system was prepared with a tunable set of neutral-density filters in close contact with the target. By gradually increasing the attenuation of the object arm, an effective reduction in the $r(x)$ parameter is achieved. This involves two key considerations:

i. Strictly, this is a reduction in the value of α_o instead of $t(x)$; however, as $r(x) = \frac{\alpha_o t(x)}{\alpha_r A(x)}$, the net effect is equivalent as long as the values for α_r, $t(x)$, and $A(x)$ are kept constant.
ii. To ensure that this approach truly emulates reductions in $t(x)$, the value of $[I_m]_{max}$, as given by Eq.(11), must also be kept constant. By configuring all the camera parameters before introducing either the sample or any neutral-density filter, and keeping them unchanged throughout the experiment, the $[I_m]_{max}$ is ensured to be taken for $r_\alpha \approx 1$.

Under these considerations, holograms from the calibrated phase target were taken at three different levels of attenuation. To measure the reduced value of $r(x)$, which represents changes in $t(x)$ for the herein-

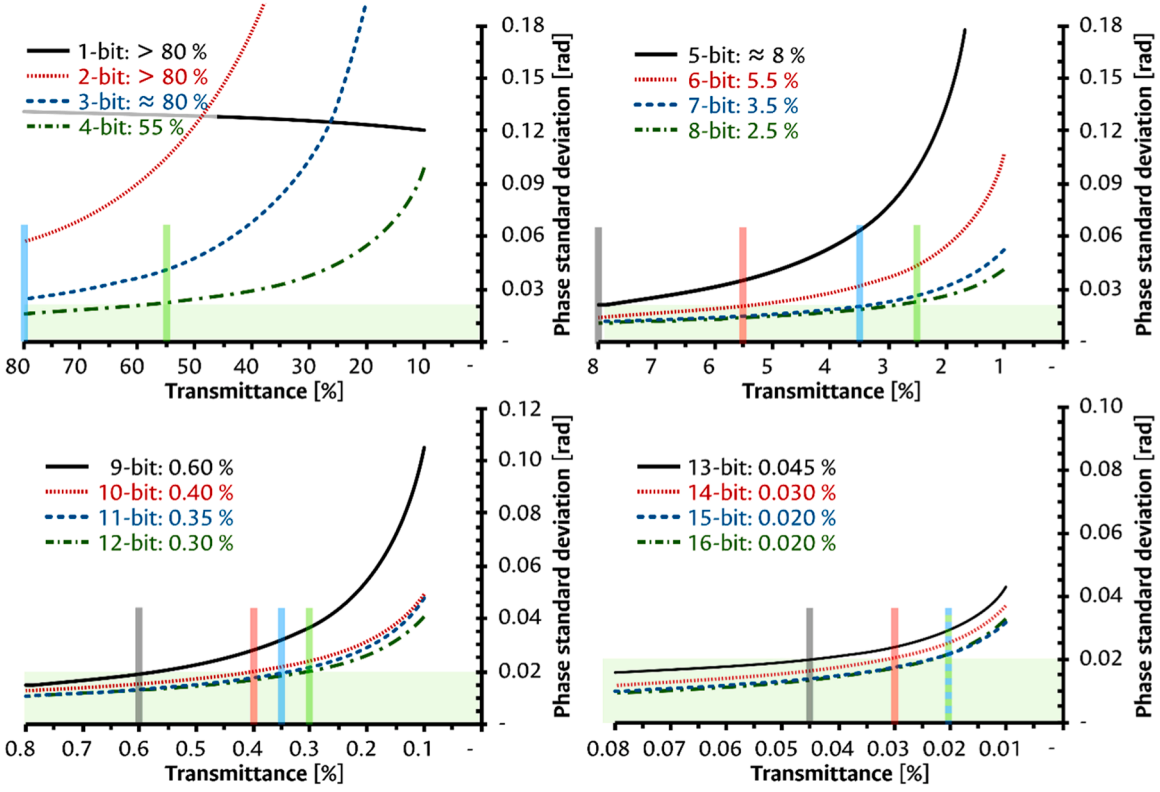

Fig. 4. Determination of transmittance limit by numerical simulation of a phase object with variable opacity. The vertical color bars mark the limit transmittance for each bit depth.

developed model, two additional images were taken at each attenuation case: one of the object intensity and one of the reference intensity, mechanically blocking the other beam in each case. The former yields a quantized measure of $|\alpha_o t(x)|^2$, while the latter likewise measures $|\alpha_r A(x)|^2$; thus, by taking the square root of the coefficient between these two measurements, an estimation of the $r(x)$ parameter can be obtained.

Average $r(x)$ measurements of 81.2 %, 7.8 %, and 0.6 % were obtained for the three attenuation cases on this sample. The corresponding phase maps, as retrieved from each of these holograms, are presented in Fig. 5 in that same order. To validate the preservation of accurate QPI measurements after the attenuation, a line plot was taken over a curved path of constant radius at the same position for the three retrieved images, marked by a color line overlaid on the phase maps in that same figure. Using the widely known relation [3]

$$\Delta h = \frac{\lambda \Delta\phi}{2\pi\left(n_{sample} - n_{air}\right)}, \tag{17}$$

the phase delay measurements $\Delta\phi$ are transformed into height differences Δh for the given illumination wavelength $\lambda = 633$ nm and the refractive index of the sample $n_{sample} = 1.52$. The resulting measurements for all three cases adequately conform to the expected value of 200 nm, which is represented in the plot of Fig. 5 by a shaded region. By direct comparison of the line plots in this figure, it is seen that the quantitative measurements are well preserved under severe reduction in the $r(x)$ parameter. The only noticeable difference is the noise level of the reconstruction. However, such an effect is to be expected, as at lower object intensities, its information gets increasingly closer to the electronic noise level of the digital detector.

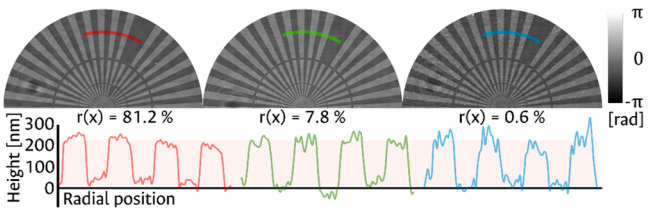

Fig. 5. Experimental imaging of a calibrated phase target at three different levels of $r(x)$ using a 16-bit camera. While there is an increase in the noise level at reduced transmittances, the quantitative measurements are mostly unaffected.

This observation was then further validated with a non-calibrated sample for which there are no known reference values, but whose intrinsic transmittance inhomogeneities pose a challenge to the DHM system. For this evaluation, a commercially prepared slide of a honeybee mouth was used. As presented in panel (a) of Fig. 6, the bright-field image shows that the sample has regions of varied degrees of transmittance, ranging from highly transmissive to almost opaque. Three interest zones with opaque features were selected, as marked by the red squares in the same panel. Panels (b), (e), and (h), show a magnified view of these zones, as acquired by a conventional optical microscope. These same portions of the sample were then imaged using the same DHM system as the previous sample. The resulting holograms acquired with this setup are illustrated in panels (c), (f), and (i) of Fig. 6. At each of the shown holograms, the overlay labels indicate the average value of the $r(x)$ parameter in the X-marked regions, calculated from intensity recordings of the object and reference waves as described for the calibrated phase target. As expected, the fringe contrast of the interference pattern is severely degraded at the lower transmittance values. The accompanying insets of panel (c) further show this reduction, with a magnified view of the fringes in a background region, and in the selected 5 %, 4 %, and 1 % regions, in that order. In the last case, the pattern is barely visible.

Notwithstanding the poor contrast of the fringes in the low-transmittance areas, the use of a 16-bit camera should allow the retrieval of phase information from regions below the 1 % transmittance threshold. Indeed, as can be seen in the phase maps from panels (d), (g),

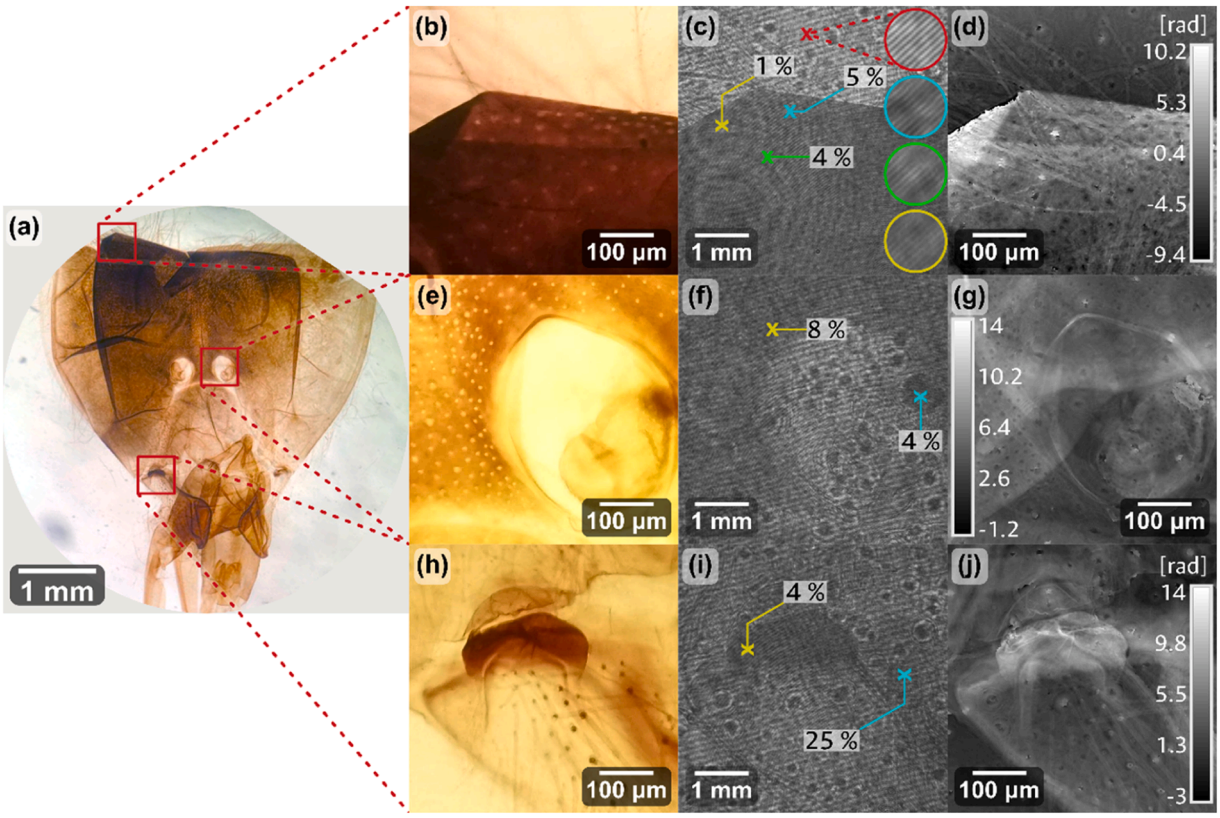

Fig. 6. Experimental imaging of a honeybee mouth. (a) Bright-field image of the sample. (b,e,h) Optical microscope images of selected zones with quasi-opaque features, and (c,f,i) their respective digital holograms where the overlaid values correspond to the average transmittance of each marked region. (d,g,j) Quantitative phase images reconstructed from each hologram.

and (j), the reconstructed information is free from the numerical-noise artifacts that could be expected from an ill-recorded hologram. Instead, the full details of the sample are retrieved. It must be noted that a direct comparison between these QPI maps and the brightfield images in panels (b), (e), and (h) is not appropriate. While they correspond to the same regions of the sample, the information that they convey is completely different. The brightfield images are used as a visual guide to the overall structure of the sample, and to convey the stark

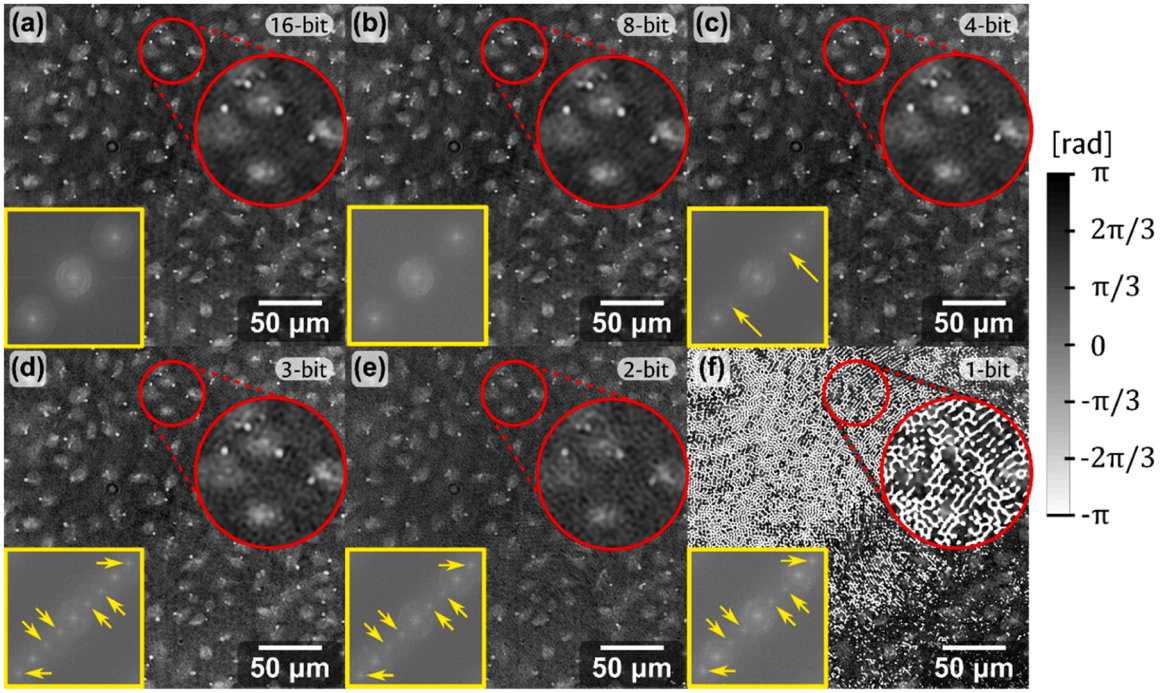

Fig. 7. Phase map of an endothelial cells sample retrieved from a hologram represented in (a) 16-bit, (b) 8-bit, (c) 4-bit, (d) 3-bit, (e) 2-bit, and (f) 1-bit. The accompanying inset in each panel shows the Fourier spectrum of the corresponding hologram. The color scale bar applies equally to all panels.

inhomogeneity in the light transmittance across the sample.

To verify the second observation, the single-shot DHM setup from the previous experiment but changing the microscope objective to a 20x/0.4 piece, was used to record a 16-bit hologram of a commercial slide of endothelial cells. Being translucent biological specimens, they can be considered to have an effective transmittance of almost 100 %. Consequently, hologram recordings of bit depths as low as $b = 3$ should be able to adequately code their phase information. The 16-bit experimental hologram was thus rescaled into new representations varying from 16-bit to 1-bit of intensity quantization. The phase map of the cell slide was then retrieved from each hologram, from which the main results are summarized in Fig. 7. Panel (a) shows the reconstruction from the 16-bit hologram, which constitutes the best-case phase map. The phase images extracted from all the reduced cases between the 16-bit and a 4-bit representation yield almost identical results, without any noticeable affectation on the retrieved information. While it is highly unlikely that any modern DHM will be equipped with a sensor with less than 8 bits, this possibility of changing the representation of the original 16-bit hologram into an image of only 4 bits without significant detriment to the retrieved QPI map opens new development avenues for compression algorithms.

This can be verified in panels (b) and (c) from the same figure, which illustrate the phase maps obtained from the 8-bit and 4-bit cases, respectively. However, by comparing the Fourier spectrum of these holograms, shown in the accompanying insets of each panel of Fig. 7, the emergence of the additional Fourier order in the 4-bit hologram can be noticed. These undesirable replicas can be attributed to the increasingly-distorted sampling conditions of the hologram, which gradually transfer more power of the spectrum into the aliases of the ill-sampled frequency. Further reduction in the bit-depth of the hologram representation is thus inevitably accompanied by increased power allocation on these replicas, which in turn introduces noise to the reconstruction and hinders the sample's information. This can be seen in panels (d) and (e), which show the phase maps recovered from the 3-bit and 2-bit representations of the hologram. While the overall information can be identified, it is severely distorted by noise. Likewise, the accompanying insets show the now visible presence of additional replicas in the Fourier spectrum. Finally, panel (f) shows the phase map obtained from the 1-bit hologram. In this case, the specimens are completely obstructed by the noise, and almost none of the retrieved information remains usable.

Similar to the experimental results for the first observation, there is not a known value for the QPI measurements of the selected endothelial cells sample. Thus, while the results in Fig. 7 allow a preliminary validation of the QPI information preservation, a quantitative study is desirable. To do so, the same element of the calibrated phase target was used. A 16-bit hologram of the fully translucent object was recorded in the DHM system and then rescaled into new bit-depth representations under the same parameters used for the endothelial cells. The retrieved QPI maps are summarized in Fig. 8 for the original 16-bit case, and the reduced representations of 8 bits, 4 bits, and 2 bits. By visually comparing the original phase map and the one retrieved from the 4-bit hologram, it is readily seen that the overall information is unaffected. This is further confirmed by the accompanying line plots, taken over a constant-radius path, where the nominal height of 200 nm is consistently retrieved for the first three cases. The transformation of the phase measurements into height information was performed in the same manner as described for Fig. 5. The 2-bit case also supports the previous result from the endothelial cell slide. While the line plot shows that the overall trend is consistent with the expected value, the information is severely degraded by noise and makes unfeasible the use of the QPI information.

The above-summarized experimental results confirm the two main predictions of the model; namely: that quantitative phase images from highly opaque regions of a transmission sample can be successfully obtained with a high-bit-depth camera, and that phase maps from a translucent sample can be retrieved from holograms with a low-bit-depth digital representation. It must be noted that all the experimentally retrieved QPI maps are presented as directly obtained from the reconstruction process of the corresponding holograms. No noise reduction or contrast enhancement algorithms were applied to avoid introducing experimental biases to the validation. The presented images show the raw capabilities of the described DHM system under these unusual operation conditions; thus, an experimental application of these observations can expect enhanced-quality reconstructions if such algorithms are employed.

5. Conclusions

Digital Holographic Microscopy (DHM) is one of the most utilized technologies to perform Quantitative Phase Imaging (QPI), due to its simplicity, robustness, and wide availability of both commercial and non-profit tools for its implementation. When using DHM for QPI analysis of transmissive samples, it is typically assumed that the successful recording of a digital hologram from which the complex-valued wavefield can be later retrieved depends on the targets being transparent or semi-transparent. However, the limit of sample transmittance after which the QPI retrieval is unfeasible has not been studied.

This work presents a study on the performance limits of single-shot off-axis DHM for the QPI analysis of samples with extreme conditions of transmittance, and its relation to the number of bits utilized for the digital recording. A theoretical model of the recording process was developed and implemented in a publicly available script. With this tool, the performance limits can be estimated as a function of the intensity relation of the interferometer arms, the transmittance of the sample, the coherence degree of the illumination, and the bit-depth of the digital camera. The model predicts that, for the commonly available cameras, DHM can perform well even with almost opaque samples, and that holograms from translucent samples could be represented in low bit depths without noticeable detriment. Particularly, for any camera beyond 8 bits, transmittances below 1 % should yield holograms from which a QPI map could be successfully retrieved.

The model predictions were contrasted with a realistic DHM-imaging platform used to generate holograms for varying degrees of sample transmittance with a fixed phase distribution. By comparing the deviation of the retrieved phase values against the ground truth, the previous observations were confirmed. Finally, these predictions were validated

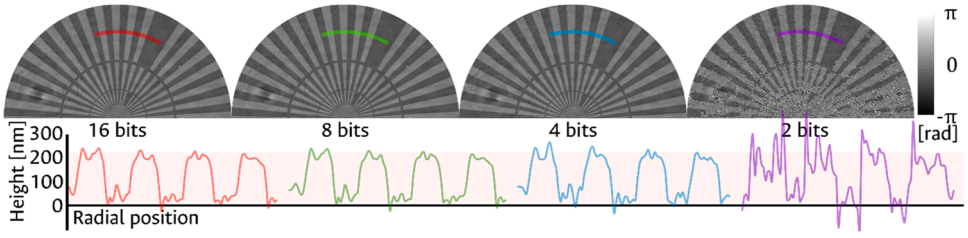

Fig. 8. QPI maps from a calibrated phase target retrieved from holograms with varying bit depth. The height measurements are unaltered down to a 4-bit representation.

on three experimental samples: a calibrated phase target, a honeybee mouthpiece, and an endothelial cells slide. The results confirmed that QPI maps could be retrieved from highly opaque regions, with transmittance below 1 %, using a 16-bit camera and that holograms from translucent regions, with almost 100 % transmittance, could be remapped into very low bit-depths without losing the ability to retrieve the phase information.

Data Availability

The data that support the findings of this study are available from the corresponding author upon reasonable request.

CRediT authorship contribution statement

C. Buitrago-Duque: Conceptualization, Methodology, Software, Validation, Data curation, Writing – original draft, Visualization. **J. Garcia-Sucerquia:** Conceptualization, Methodology, Writing – original draft, Supervision. **M. Martínez-Corral:** Conceptualization, Resources, Writing – review & editing, Funding acquisition. **E. Sánchez-Ortiga:** Conceptualization, Methodology, Validation, Writing – review & editing.

Declaration of Competing Interest

The authors declare that they have no known competing financial interests or personal relationships that could have appeared to influence the work reported in this paper.

Acknowledgments

This work was funded in part by Generalitat Valenciana, Spain, through project CIPROM/2022/30. C. Buitrago-Duque thanks the Universitat de València for its support through the “Beca Jóvenes Investigadores 2022”. J. Garcia-Sucerquia thanks Fundación Carolina and Universidad Nacional de Colombia for their support in finishing this work.

References

[1] Popescu G. Quantitative phase imaging of cells and tissues. McGraw Hill Professional; 2011.
[2] Cuche E, Bevilacqua F, Depeursinge C. Digital holography for quantitative phase-contrast imaging. Opt Lett 1999;24:291–3.
[3] Marquet P, Rappaz B, Magistretti PJ, Cuche E, Emery Y, Colomb T, Depeursinge C. Digital holographic microscopy: a noninvasive contrast imaging technique allowing quantitative visualization of living cells with subwavelength axial accuracy. Opt Lett 2005;30:468.
[4] Cuche E, Marquet P, Depeursinge C. Simultaneous amplitude-contrast and quantitative phase-contrast microscopy by numerical reconstruction of Fresnel off-axis holograms. Appl Opt 1999;38:6994.
[5] Diederich B, Lachmann R, Carlstedt S, Marsikova B, Wang H, Uwurukundo X, Mosig AS, Heintzmann R. A versatile and customizable low-cost 3D-printed open standard for microscopic imaging. Nat Commun 2020;11:5979.
[6] Amann S, von Witzleben M, Breuer S. 3D-printable portable open-source platform for low-cost lens-less holographic cellular imaging. Sci Rep 2019;9:11260.
[7] Tobon-Maya H, Zapata-Valencia S, Zora-Guzmán E, Buitrago-Duque C, Garcia-Sucerquia J. Open-source, cost-effective, portable, 3D-printed digital lensless holographic microscope. Appl Opt 2021;60:A205.
[8] D. Cohoe, "DHM utilities," https://imagej.net/plugins/dhm-utilities/.
[9] Castañeda R, Trujillo C, Doblas A. pyDHM: a Python library for applications in digital holographic microscopy. PLoS One 2022;17:e0275818.
[10] Buitrago-Duque C, Garcia-Sucerquia J. Realistic simulation and real-time reconstruction of digital holographic microscopy experiments in ImageJ. Appl Opt 2022;61:B56.
[11] Kühn J, Charrière F, Colomb T, Cuche E, Montfort F, Emery Y, Marquet P, Depeursinge C. Axial sub-nanometer accuracy in digital holographic microscopy. Meas Sci Technol 2008;19.
[12] Castañeda R, Garcia-Sucerquia J. Single-shot 3D topography of reflective samples with digital holographic microscopy. Appl Opt 2018;57:A12–8.
[13] Charrière F, Marian A, Montfort F, Kuehn J, Colomb T, Cuche E, Marquet P, Depeursinge C. Cell refractive index tomography by digital holographic microscopy. Opt Lett 2006;31:178–80.
[14] Charrière F, Colomb T, Montfort F, Cuche E, Marquet P, Depeursinge C. Shot-noise influence on the reconstructed phase image signal-to-noise ratio in digital holographic microscopy. Appl Opt 2006;45:7667–73.
[15] Goodman JW. Introduction to Fourier optics. 3rd ed. Roberts & Company Publishers; 2005.
[16] Ersoy OK. Diffraction, Fourier optics and imaging. John Wiley & Sons, Inc.; 2007.
[17] Li J, Picart P. Calculating Diffraction by Fast Fourier Transform. Digital holography. 2012. p. 77–114.
[18] Antkowiak M, Callens N, Yourassowsky C, Dubois F. Extended focused imaging of a microparticle field with digital holographic microscopy. Opt Lett 2008;33:1626.
[19] Colomb T, Pavillon N, Kühn J, Cuche E, Depeursinge C, Emery Y. Extended depth-of-focus by digital holographic microscopy. Opt Lett 2010;35:1840–2.
[20] Zhu Y, Yeung CHang, Lam EY. Digital holographic imaging and classification of microplastics using deep transfer learning. Appl Opt 2021;60:A38–47.
[21] Tian L, Loomis N, Domínguez-Caballero JA, Barbastathis G. Quantitative measurement of size and three-dimensional position of fast-moving bubbles in air-water mixture flows using digital holography. Appl Opt 2010;49:1549–54.
[22] Verrier N, Atlan M. Off-axis digital hologram reconstruction: some practical considerations. Appl Opt 2011;50:H136–46.
[23] Sánchez-Ortiga E, Doblas A, Saavedra G, Martínez-Corral M, Garcia-Sucerquia J. Off-axis digital holographic microscopy: practical design parameters for operating at diffraction limit. Appl Opt 2014;53:2058.
[24] Sánchez-Ortiga E, Doblas A, Martínez-Corral M, Saavedra G, Garcia-Sucerquia J. Aberration compensation for objective phase curvature in phase holographic microscopy: comment. Opt Lett 2014;39:417.
[25] Doblas A, Sánchez-Ortiga E, Martínez-Corral M, Saavedra G, Andrés P, Garcia-Sucerquia J. Shift-variant digital holographic microscopy: inaccuracies in quantitative phase imaging. Opt Lett 2013;38:1352–4.
[26] Takeda M, Ina H, Kobayashi S. Fourier-transform method of fringe-pattern analysis for computer-based topography and interferometry. J Opt Soc Am 1982;72:156.
[27] Cuche E, Marquet P, Depeursinge C. Spatial filtering for zero-order and twin-image elimination in digital off-axis holography. Appl Opt 2000;39:4070–5.
[28] Trujillo C, Castañeda R, Piedrahita-Quintero P, Garcia-Sucerquia J. Full compensation of quantitative phase images of digital holographic microscopy using GPU. Imaging and applied optics 2018 (3D, AO, AIO, COSI, DH, IS, LACSEA, LS&C, MATH, PCAOP). Optical Society of America; 2018. OSA Technical DigestVol. Part F100-, p. DTh2C.4.
[29] C. Buitrago-Duque and J. Garcia-Sucerquia, "Digital Holographic Microscopy (DHM) - An ImageJ Plugin," https://unal-optodigital.github.io/DHM/.
[30] Hariharan P. Optical holography: principles, techniques, and applications. 2nd ed. Cambridge University Press; 1996.
[31] Tippie AE, Fienup JR. Weak-object image reconstructions with single-shot digital holography. Biomedical optics and 3-D imaging. Optical Society of America; 2012DM4C.5.
[32] Gross M, Atlan M, Absil E. Noise and aliases in off-axis and phase-shifting holography. Appl Opt 2008;47:1757.
[33] Atlan M, Gross M, Desbiolles P, Absil E, Tessier G, Coppey-Moisan M. Heterodyne holographic microscopy of gold particles. Opt Lett 2008;33:500–2.
[34] Verpillat F, Joud F, Atlan M, Gross M. Digital holography at shot noise level. J Disp Technol 2010;6:455–64.
[35] Charriére F, Rappaz B, Kühn J, Colomb T, Marquet P, Depeursinge C. Influence of shot noise on phase measurement accuracy in digital holographic microscopy. Opt Express 2007;15:8818–31.
[36] Mirecki B, Rogalski M, Arcab P, Rogujski P, Stanaszek L, MichałJózwik, Trusiak M. Low-intensity illumination for lensless digital holographic microscopy with minimized sample interaction. Biomed Opt Express 2022;13:5667–82.
[37] Picart P, Juan-chang L. Digital holography. Wiley; 2012.
[38] Gåsvik KJ. Optical metrology. 3rd ed. John Wiley & Sons; 2002.
[39] Boreman GD. Modulation transfer function in optical and electro-optical systems. SPIE; 2001.
[40] Hecht E. Optics. 4th ed. Addison-Wesley; 2012.
[41] C. Buitrago-Duque, J. Garcia-Sucerquia, M. Martinez-Corral, and E. Sánchez-Ortiga, "Transmittance limit for digital holographic microscopy," https://www.mathworks.com/matlabcentral/fileexchange/124450-transmittance-limit-for-digital-holographic-microscopy.
[42] Jiao S, Jin Z, Chang C, Zhou C, Zou W, Li X. Compression of phase-only holograms with JPEG standard and deep learning. Appl. Sci. 2018;8:1258.
[43] F. Dufaux, Y. Xing, B. Pesquet-Popescu, and P. Schelkens, "Compression of digital holographic data: an overview," in A. G. Tescher, editor (2015), p. 95990I.
[44] Buitrago-Duque C, Garcia-Sucerquia J. Realistic modeling of digital holographic microscopy. Opt Eng 2020;59:1.
[45] Benchmark Technologies, "Quantitative phase microscopy target," https://www.benchmarktech.com/quantitativephasemicroscop.